Effect of ceria and zirconia promotors on Ni/SBA-15 catalysts for coking and sintering resistant steam reforming of propylene glycol in microreactors

Vetrivel Shanmugam [a],[*], Ralf Zapf [b], Stefan Neuberg [b], Volker Hessel [a], Gunther Kolb [a],[b],[*]

[a] Department of Chemical Engineering and Chemistry, Micro Flow Chemistry and Process Technology, Eindhoven University of Technology, P.O. Box 513, 5600 MB Eindhoven, The Netherlands
[b] Fraunhofer ICT-IMM, Division of Energy and Chemical Technology, Carl-Zeiss-Straße 18-20, 55129 Mainz, Germany

ARTICLE INFO

ABSTRACT

Highly dispersed and size controlled Ni nanoparticles in CeO_2, ZrO_2 and CeO_2-ZrO_2 promoted mesoporous SBA-15 silica were achieved with the aid of treatment by ultrasound. The catalysts were characterized systematically to investigate their morphological structure and surface properties. It was found that Ni nanoparticles with an average particle size of about 4.5 nm have been successfully embedded in the nanochannels of SBA-15 with a homogeneous distribution. The incorporated CeO_2 and ZrO_2 promotors effectively controlled the size of the Ni particles via strong Ni-promotor interaction, leading to well dispersed Ni particles in the confined nanochannels of SBA-15. The catalysts thus obtained were applied for steam reforming of propylene glycol in continuous flow microchannel reactors, which reduce the heat and mass transfer limitations when operating them under conditions of highly endothermic reforming reactions. The CeO_2, ZrO_2 and CeO_2-ZrO_2 promoted Ni/SBA-15 catalysts exhibited superior activity and enhanced long-term stability compared to the Ni/SBA-15 catalyst without promotor addition. This can be attributed to the strong interaction between Ni and the promotors and the confinement effect of the SBA-15 support restricted the sintering of Ni particles. The surface oxygen species arising from CeO_2 and ZrO_2 contributed to suppressing the carbon deposition effectively, leading to a consistent catalytic performance during propylene glycol reforming.

© 2016 Published by Elsevier B.V.

1. Introduction

Hydrogen is considered as an emerging energy carrier with significant environmental benefits, due to the fact that its combustion is free of pollutants [1]. It can be produced from different sources through different processes, but one feasible way is steam reforming of alcohols such as methanol, ethanol, ethylene glycol, propanol and glycerol [2–7]. Especially propylene glycol is an attractive fuel for specific mobile applications in the aerospace environment owing to its not existing toxicity and, when mixed with sufficient amounts of water, its inflammability. However, the major problem of hydrogen production from propylene glycol via the steam reforming reaction is catalyst deactivation caused by sintering and carbon deposition. Nickel supported on ordered mesoporous oxides has been investigated extensively in high-temperature reforming reactions [8–10]. Wang et al. reported about ordered mesoporous Ni-Ce-Al oxides catalysts and their performance in methane reforming reactions [11,12]. The effect of Ni in mesoporous Ni-Al_2O_3-ZrO_2 oxides have been investigated by steam reforming of ethanol [13]. However, the sintering of Ni nanoparticles (NPs) reduces the overall surface area and active sites that becomes more vulnerable to the formation of coke and simultaneously deactivate the catalysts [14,15]. The role of the mesopores in ordered mesoporous Ni–Mg–Al oxide catalysts is to prevent Ni metal from sintering and coke accumulation under severe reaction conditions of methane steam reforming [16]. Shuirong Li and Jinlong Gong reported strategies for improving the performance and stability of Ni-based catalysts for reforming reactions [17]. Owing to the confinement effect of pore walls and its high thermal stability, well-ordered mesoporous SBA-15 silica has been highlighted as an ideal host support for holding the Ni NPs, which can

* Corresponding authors.
E-mail addresses: V.Shanmugam@tue.nl (V. Shanmugam),
Gunther.Kolb@imm.fraunhofer.de (G. Kolb).

be confined in the pore channel of SBA-15 and partially maintain their dispersion [18–20]. Highly dispersed and thermally stabilized small size Ni NPs have the tendency to resist the sintering and suppress the coke deposition. Inspired by the advantages of small size Ni particles on resistance to carbon deposition, numerous publications deal with controlling the size of Ni particles [21–23].

The addition of second metal oxides to the support as a promotor is capable of controlling the particle size and enhance the dispersion through stabilizing the Ni particles against thermal sintering due to the strong metal-support interaction [24–26]. In recent studies, several metal oxides such as CuO [14,27,28], Mo [29,30], MgO [6,31], CeO_2 [25,26,32–36], ZrO_2 [33,34], La_2O_3 [37] and CaO [6] have been frequently introduced as a promotor to stabilize the Ni NPs on the support. Among them, ceria and/or zirconia were found to be excellent promotors to stabilize the Ni particles due to their high thermal stability while they remarkably enhance the Ni particles dispersion. In addition, they act as strong inhibitor for coke formation because of their higher oxygen storage capacity (OSC), which has the ability to adsorb and release oxygen under oxidizing and reducing conditions, respectively [33]. Previous investigation indicate that ceria oxide could promote the dispersion of Ni NPs on the silica matrix and enhance the mobility of surface oxygen species arising from the oxygen storage capacity (OSC) of CeO_2, which enhances the sintering and the coke resistance in the methane reforming reaction [32]. It has been reported that Ce modified $Ni-SiO_2$ improves the coke resistance and leads to the consistent catalytic performance in dry reforming of methane [25]. Recently, Wang et al. reported the high stability of Ce/SBA-15 supported nickel catalyst during long term testing of methane reforming [38]. The Ni loaded onto the ceria-coated SBA-15 showed superior stability compared to Ni loaded on a bare SBA-15 support in dry reforming of methane [24] and steam reforming of ethanol [26]. However, the addition of zirconia to ceria also leads to an improved oxygen storage capacity, redox properties, and thermal resistance and to higher catalytic activity [33]. The doping effect of phases such as ZrO_2, CeO_2 and $Ce_xZr_{1-x}O_2$ on Ni catalysts has been investigated in methane reforming [36,39,40], where it was found that the higher amount of oxygen vacancies near the metal particles promotes the mechanism of carbon removal from the metallic surface. Generally, this kind of ceria and zirconia promoted Ni/SBA-15 catalysts have been prepared by the incipient wetness impregnation route. It is acknowledged that ultrasonic irradiation could be a feasible synthesis route for the production of highly dispersed and uniform metal oxide particles within the pore channels of SBA-15 [41]. By using the advantages associated with the sonochemical method, we herein, achieve highly dispersed and size controlled Ni nanoparticles in CeO_2, ZrO_2 and CeO_2-ZrO_2 promoted SBA-15 silica.

To date, no studies dealing with the effect of ceria and zirconia promotors on Ni/SBA-15 catalysts in propylene glycol reforming reaction can be found in the existing literature. In our previous studies, we developed an efficient Ni/SBA-15 catalyst for hydrogen production from steam reforming of propylene glycol in microchannel reactors [42]. Compared with conventional fixed bed reactors, microchannel reactors offer advantages of improved heat and mass transfer coefficients due to high surface area to volume ratios of microchannels, lower pressure drop since microchannel reactors work under laminar flow conditions, and providing built-in safety since a large gas hold-up is avoided [43,44]. In this work, we further extend our research in order to explore the effect of ceria and zirconia in Ni/SBA-15 on the stability and catalytic activity in the steam reforming of propylene glycol reaction in microchannel reactors. We also investigated the coke formation behavior of spent Ni/SBA-15 catalysts with and without ceria and zirconia promotion.

2. Experimental

2.1. Catalysts preparation

Mesoporous silica SBA-15 was synthesized by the hydrothermal method as reported by Zhao et al. [45]. 1 g of SBA-15 was mixed with an aqueous solution of $Ce(NO_3)_3 \cdot 6H_2O$ (3 wt%), $Zr(NO_3)_4 \cdot 5H_2O$ (3 wt%) and Ceria with zirconia (1.5 wt% Ce + 1.5 wt% Zr) to immobilize the CeO_2, ZrO_2 and CeO_2-ZrO_2 separately into mesoporous nanochannels by ultrasonic irradiation for 1 h (Branson, 100 W 42 kHz). The samples were dried and calcined at 450 °C for 4 h in air. Then, the CeO_2-SBA-15, ZrO_2-SBA-15 and CeO_2ZrO_2-SBA-15 powders were mixed with an aqueous solution of $Ni(NO_3)_3 \cdot 6H_2O$ (12 wt%) and the slurry was sonicated for 1 h to achieve Ni/CeO_2-SBA-15, Ni/ZrO_2-SBA-15 and Ni/CeO_2ZrO_2-SBA-15. Finally, the catalysts were dried overnight and calcined at 450 °C for 6 h. Similarly, Ni/SBA-15 catalyst was prepared without addition of ceria or zirconia. The ceria, zirconia and nickel content in catalysts was determined by XRF.

For comparison, we also prepared CuO (3 wt%), and CuO with CeO_2 (1.5 wt% Cu + 1.5 wt% Ce) promoted Ni/SBA-15 (12 wt% of Ni) catalysts by following the same procedure. The catalysts are named as Ni/CuO-SBA-15 and Ni/CuOCeO_2-SBA-15.

2.2. Catalysts coating

The catalysts were coated onto stainless steel microchannels by applying the wash coating technique with an aqueous suspension containing polyvinyl alcohol (PVA) as a binder and the catalyst powder [46]. First PVA was dissolved in water under constant stirring at 65 °C for 3 h. Then the catalyst powder was added and the mixture was stirred for another 3 h at the same temperature. A homogenous suspension was achieved after stirring the mixture for 2 or 3 days at room temperature. The microchannels of the reactors were filled with the as-prepared suspension and excess suspension was wiped off. Finally, the coated microchannel plates were dried at room temperature and calcined at 450 °C for 6 h.

2.3. Catalysts characterization

Powder X-ray diffraction (XRD) patterns were collected on a Rigaku multipurpose X-ray diffraction system. N_2 adsorption-desorption isotherms were measured at 77 K on a Micromeritics Tristar II (surface area and porosity) analyzer. The calcined sample was degassed at 150 °C for four hours before measurements. The Brunauer-Emmett-Teller (BET) method in the relative pressure range of $P/P_0 = 0.0–1.0$ was employed to obtain specific surface areas. The pore size distribution was obtained from the analysis of the adsorption branch of the isotherm by the Barrett-Joyner-Halenda (BJH) method. Thermogravimetric analysis (TGA) was carried out on a Perkin Elmer TGA7 thermogravimetric analyzer with a heating rate of 10 °C/min under air in a flow of 50 ml/min. The TEM images were acquired on a FEI Tecnai microscope operating at 200 kV. To prepare samples for TEM observations, a small amount of the material was first suspended in ethanol by sonication in an ultrasonic water bath for an hour. A drop of this suspension was then placed onto the copper grids with holey carbon films, followed by drying at room temperature. The H_2-TPR measurements were carried out in a quartz tube reactor equipped with a thermal conductivity detector (TCD). First, the catalysts were pretreated at 300 °C for 60 min in a flowing stream of high-purity Argon. After cooling to room temperature, a 10% H_2 in N_2 gas mixture (25 ml/min) was introduced and the temperature was raised from room temperature to 750 °C with a rate of 10 °C min⁻¹. The TPO measurements were carried out with the same procedure of H_2-TPR. The difference was that 10% O_2 in N_2 gas mixture was

applied as carrier gas. H_2 pulse chemisorption experiments were carried out using a Micromeritics Autochem II (chemisorption analyzer). First, the catalyst was reduced in H_2 flow at 500 °C for 2 h. After the temperature reached to 40 °C, 10% H_2 in Ar was injected in pulses until no further change in the TCD signal intensity was detected.

2.4. Catalytic activity measurements

Oxidative steam reforming tests were carried out in a plug flow-type apparatus with a microchannel reactor at atmospheric pressure and a temperature at 630 °C. The water and propylene glycol mixture (S/C = 3.5) was placed in a tank under inert gas pressure as driving force for feeding a liquid mass flow controller (LMFC), and using an evaporator, the mixture was introduced into the test reactor. The test reactor has a sandwich design with two microchannel platelets being attached face to face. Each platelets carry 14 channels of 25 mm long, 500 µm wide and 250 µm deep. Each pair of platelets was coated with the developed catalysts (see 2.2) and subsequently sealed by laser welding. Inlet and outlet capillaries were attached to the microchannel reactors by laser welding as well [47,48]. A synthetic air stream was added by a gas MFC to the previously vaporized propylene glycol-water mixture in order to reach the intended atomic oxygen to carbon (O/C) ratio of 0.15. The total flow rate of vapor was 30 ml/min. Before starting the experiment, the reactor was by-passed until a stable feed composition and the desired reactor temperature were reached. The wash-coated catalysts were pre-reduced in 20% H_2/N_2 at 500 °C for 2 h prior to the catalytic test. The obtained product composition was analyzed by on-line Mass spectroscopy (MS, InProcess Instruments Online Mass Spectrometer GAM400).

3. Results and discussion

3.1. Characteristics of catalysts

Fig. 1A shows the small-angle XRD patterns of the SBA-15, Ni/SBA-15, Ni/CeO$_2$-SBA-15, Ni/ZrO$_2$-SBA-15 and Ni/CeO$_2$ZrO$_2$-SBA-15 catalysts. Each spectrum exhibited three well-resolved diffraction peaks in the region of $2\theta = 0.5$–$2.0°$, which were indexed to the (100), (110) and (200) diffractions that are characteristic of mesoporous silica materials with p6mm hexagonal symmetry [45]. When promotors and NiO were loaded onto SBA-15, the *d*-spacing of the 100 plane is decreased resulting in a shift of the d$_{100}$ peak to slightly higher angle and an attenuation in intensity. It is implying that promotors and NiO are embedded into the nanochannels and dispersed on the surface without affecting the structural order of the parent SBA-15. Fig. 1B shows the wide-angle XRD patterns of the cubic crystalline structure of NiO for all the calcined catalysts, which exhibited peaks at $2\theta \approx 37.2°$, $43.1°$, $62.8°$, $75.3°$ and $79.4°$ corresponding to the (111), (200), (220), (311) and (222) facets [49]. For Ni/CeO$_2$-SBA-15 catalyst, the CeO$_2$ peaks are observed at $2\theta \approx 28.5°$, $47.4°$, and $56.4°$, corresponding to (111), (200), (220), (311) and (222), which are characteristic of the cubic fluorite structure of CeO$_2$ [50]. In the case of Ni/ZrO$_2$-SBA-15 catalyst, a small peak appeared at $2\theta \approx 30.1°$ which was attributed to the monoclinic phase of ZrO$_2$. The CeO$_2$ and ZrO$_2$ peaks are not visible clearly for the Ni/CeO$_2$ZrO$_2$-SBA-15 catalyst due to the presence of lower amounts of ceria and zirconia. The crystal size of NiO was calculated using line broadening of Scherrer equation and the results are presented in Table 1. After reduction of catalyst in presence of hydrogen, the Ni/SBA-15 catalyst exhibits three peaks at the range of $2\theta \approx 44.4°$, $51.8°$ and $76.4°$ corresponding to the (111), (200) and (220) plans of face-centered cubic (fcc) structure for metallic nickel [51]. This observation suggests that the NiO species confined in the

nanochannels of silica could be reduced completely as metallic Ni NPs during prior reduction of the catalyst in the reforming reaction. By applying the Scherrer equation to the XRD pattern, the Ni particle size from (111) plane of reduced catalyst was calculated to about 4 nm, which is much smaller than the pore diameter of SBA-15, indicating a blockage-free confined space with small nanoparticles inside of the mesoporous nanochannels.

Fig. 2 shows the nitrogen adsorption-desorption isotherms and pore size distribution of the Ni based SBA-15 catalysts with addition of CeO$_2$ and ZrO$_2$ promotors. All of the samples exhibited type IV isotherms with well-expressed H1-type hysteresis, which is typical for mesoporous materials with one-dimensional cylindrical channels. However, all the samples comprise two hysteresis loops, which suggests that the mesoporous channels contain both cylindrical and ink-bottle shape pores because promotors and Ni particles partially filled the pores. The upper region of the hysteresis loop ranges from 0.6 to 0.8 P/Po which corresponds to the bare portion of nanochannels similar to the parent SBA-15 host [45]. The lower region of the hysteresis loop from 0.43 to 0.6 P/Po corresponds to another set of capillary condensation for N$_2$ [52]. This result suggests that the immobilizing Ni particles in the mesopores must therefore lead to a change of pore structure in the confined space. However, the hexagonally ordered structure of SBA-15 has not been destroyed. These results are in good agreement with those results obtained by low-angle XRD patterns.

The pore size distribution of all samples, which are calculated from the N$_2$-adsorption isotherms according to the Barrett-Joyner-Halenda (BJH) method, show bimodal pore size distributions. It is related to the two-step feature observed in the desorption branch of the isotherm. The textural properties that were obtained from the N$_2$ adsorption-desorption measurements are summarized in Table 1. As seen in the table, decreasing surface area and pore volume were both observed after loading of promotors and Ni, suggesting the incorporation of promotors and the Ni particles into the pores of SBA-15. For all the catalysts, the original pore is centered at 5.7 nm, which is responsible for the hysteresis at P/Po 0.6–0.8 of typical open-ended cylindrical mesopores of pure SBA-15 host. After Ni loading into the mesoporous SBA-15 via ultrasonic irradiation, the additional pore is appearing at 3.7 nm associated with the hysteresis at P/Po 0.43–0.6, which is suggestive of ink-bottle type mesopores resulting from the Ni particles deposition inside of the nanochannels. Ink-bottle mesopores are characterized by a small neck in the pore through which the volume between two Ni NPs would be accessible [52,53]. The formation of this new pore at 3.7 nm and the observed loss in pore volume confirms that Ni particles were located inside the nanochannels mesoporous silica [41]. However, the Ni particles did not block the mesoporous nanochannels, which ensured that the catalysts possess high surface area and large pore volume. The catalysts Ni/CuO-SBA-15 and Ni/CuOCeO$_2$-SBA-15, which were prepared for comparison, also show two pores at 3.7 and 5.7 nm respectively (Fig. S1A&B-inset). However, the intensity of the open-ended cylindrical mesopore (5.7 nm) is higher for Ni/CuO-SBA-15 catalyst suggesting that a lower amount of Ni particles is immobilized into the nanochannels mesoporous silica.

The XP Ni 2p$_{3/2}$ spectra of calcined Ni/CeO$_2$-SBA-15, Ni/ZrO$_2$-SBA-15 and Ni/CeO$_2$ZrO$_2$-SBA-15 catalysts are shown in Fig. 3. The catalysts exhibited a Ni 2p$_{3/2}$ main peak at 854.4–856.6 eV with a shake-up satellite peak around 861.7 eV. The typical Ni 2p$_{3/2}$ peaks at 854.5 and 856.6 eV were attributed to NiO and Ni$_2$O$_3$ species interacting with the mesoporous SBA-15 support [54]. H$_2$-TPR profiles were employed to investigate the reducibility of Ni/SBA-15, Ni/CeO$_2$-SBA-15, Ni/ZrO$_2$-SBA-15 and Ni/CeO$_2$ZrO$_2$-SBA-15 catalysts, and the results are shown in Fig. 4. It shows two reduction peaks for all the catalysts indicating the presence of two different types of NiO species anchored to the silica support. The Ni^{2+} is reduced to Ni^0 without going through any intermediate oxides,
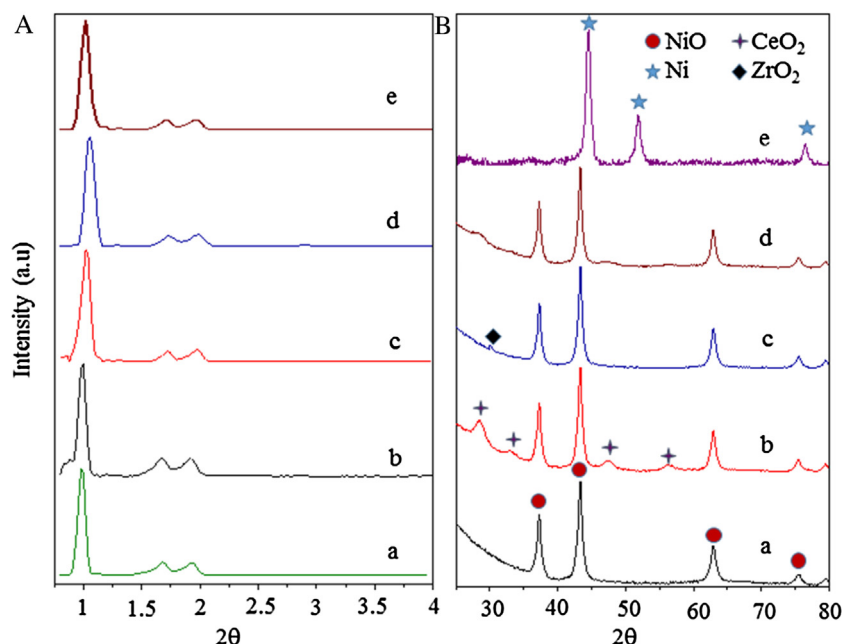
Fig. 1. (A) Low-angle XRD of (a) SBA-15, (b) Ni/SBA-15, (c) Ni/CeO$_2$-SBA-15, (d) Ni/ZrO$_2$-SBA-15 and (e) Ni/CeO$_2$ZrO$_2$-SBA-15 and (B) Wide-angle XRD of (a) Ni/SBA-15, (b) Ni/CeO$_2$-SBA-15, (c) Ni/ZrO$_2$-SBA-15, (d) Ni/CeO$_2$ZrO$_2$-SBA-15 and (e) Ni/SBA-15 reduced in presence of H$_2$.

Table 1
Textural properties of ceria and/or zirconia promoted Ni/SBA-15 catalysts.

Catalysts	A_{BET}/m^{2}g^{-1}[a]	V_p/cm^{3}g^{-1}[b]	Average pore size (nm)	Average NiO size (nm)[c]	NiO Dispersion (%)[d]	Metal content Ni/Ce/Zr (wt% ± 0.3)[e]
SBA-15	799	10.9	5.7	–	–	–
Ni/SBA-15	582	10.7	4.6	8.7	9.6	11.9
Ni/CeO$_2$-SBA-15	453	10.6	4.7	5.6	18.7	11.8/2.71
Ni/ZrO$_2$-SBA-15	474	10.6	4.8	5.4	16.6	11.7/2.46
Ni/CeO$_2$ZrO$_2$-SBA-15	479	10.6	4.8	6.4	17.3	11.9/1.46/1.26

[a] A_{BET} = BET surface area.
[b] V_p = total pore volume.
[c] Calculated from XRD.
[d] H$_2$ Pulse chemisorption.
[e] The metallic contents were measured by XRF.

and therefore H$_2$ consumption peaks for different NiO species appear at different temperature [55]. The first peak is assigned to the reduction of surface bulk NiO species located on the outer surface of mesoporous silica with a weak interaction, while the second peak can be ascribed to the reduction of NiO species confined within the nanochannels with strong interaction with the silica support [21,25]. In the case of Ni/CeO$_2$-SBA-15 catalyst, some changes of reduction patterns are observed due to introduction of CeO$_2$ before Ni loading. The first reduction peak shifts from 378 °C to 306 °C indicating that smaller NiO species are present on the outside of the silica surface and easier to be reduced, and the second reduction peak shifts from 530 °C to 482 °C, demonstrating the high mobility and activity of surface oxygen species on Ni/CeO$_2$-SBA-15 catalyst [32]. Moreover, the intensity of the second H$_2$ consumption peak becomes stronger suggesting that a higher amount of NiO species was delivered into ceria promoted SBA-15 nanochannels with strong interaction between Ni and CeO$_2$. The downward peak shift is caused by the strengthened interaction between Ni and ceria, which is considerably beneficial to resist the sintering of Ni during the reforming reaction. The incorporation of NiO into ceria promoted SBA-15 led to the formation of Ni–Ce–O species and the enhancement of the lattice distortion of ceria and Ni dispersion facilitate the reduction behavior of Ni/CeO$_2$-SBA-15 [24]. Similar reduction behavior was observed for both Ni/ZrO$_2$-SBA-15 and Ni/CeO$_2$ZrO$_2$-SBA-15 catalysts. However, the

downward peak shift is lower in Ni/ZrO$_2$-SBA-15 and Ni/CeO$_2$ZrO$_2$-SBA-15 than in Ni/CeO$_2$-SBA-15, revealing that the ZrO$_2$ possesses lower surface active oxygen compared to CeO$_2$. Overall, the H$_2$-TPR results suggested that the addition of ceria and zirconia in SBA-15 resulted in more highly dispersed Ni NPs in intimate contact with the support, preventing the sintering of Ni NPs in the PG steam reforming reaction. In addition, the high mobility and activity of surface oxygen species due to the redox property of ceria and zirconia and the formation of an oxygen vacancy could react with carbon arising from PG reforming reaction and reduce the carbon deposition through the gasification process of coke. The catalysts Ni/CuO-SBA-15 and Ni/CuOCeO$_2$-SBA-15, which were prepared for comparison and their results of which are presented in Fig. S1C, show two reduction peaks with maxima between 180 and 350 °C. The main peak is attributed to NiO reduction, while the small peak at low temperature is associated to CuO reduction [27]. Unfavorably, the addition of copper decreases the nickel reduction temperature due to the presence of a higher amount of NiO species on the external surface of the silica, and reduces the interaction of Ni with the support. Comparing with Ni/CuO-SBA-15, the peaks are shifted to a slightly higher temperature for Ni/CuOCeO$_2$-SBA-15 catalyst due to the presence of a small amount of ceria.

TEM analysis were employed to investigate the morphology of Ni NPs and their distribution, and the results are shown in Fig. 5.
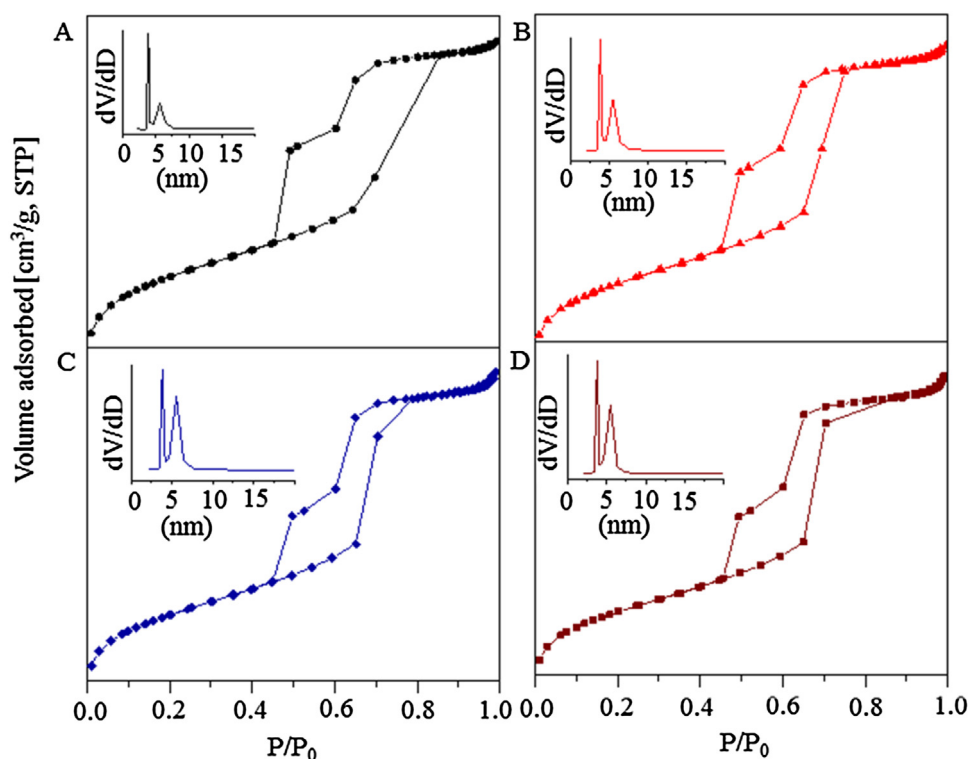
Fig. 2. Nitrogen adsorption-desorption isotherms with pore size distribution of (A) Ni/SBA-15, (B) Ni/CeO$_2$-SBA-15, (C) Ni/ZrO$_2$-SBA-15 and (D) Ni/CeO$_2$ZrO$_2$-SBA-15 catalysts.

The presence of nickel and ceria are confirmed by XPS and SEM with EDX (Fig. S2&S3). The TEM images and corresponding histogram of the Ni/CeO$_2$-SBA-15 catalyst show that the Ni particles are well dispersed and uniformly distributed throughout the nanochannels of mesoporous SBA-15 with an average particle size of about 4.5 nm. The smaller size of the Ni particles is considerably beneficial to enhance the sintering resistance of the catalyst due to the confinement effect arising from the mesoporous wall of silica support [21]. The controlled size and distribution of the Ni particles originates from the presence of CeO$_2$ in the nanochannels of silica. When ceria is mixed with SBA-15, it was first dispersed uniformly in the mesoporous silica surface and the strong affinity of Ce^{3+} was suggested to act as a barrier to prevent the intimate contact to Ni and Si owing to the strong interaction between Ni and Ce, resulting in highly dispersed Ni NPs. Similarly, Ni/ZrO$_2$-SBA-15 and Ni/CeO$_2$ZrO$_2$-SBA-15 catalysts also show higher dispersion of Ni NPs with an average particle size of 4.8 and 4.7 (Fig. 5B and C) respectively. For Ni/SBA-15 catalyst (Fig. 5D), the presence of Ni was confirmed by SEM and EDX analysis (Fig. S4), the dispersion of the Ni NPs seems to be slightly lower than for the ceria and zirconia promoted Ni/SBA-15 catalysts. The corresponding histogram of this catalyst exhibits the Ni particle size distribution which has a wide range from 2.5 nm to 9 nm, and a maximum centered at about 5.2 nm. Moreover, it shows some agglomerated particles, which could be placed over the external surface of silica. H$_2$ pulse chemisorption results also indicated a higher Ni dispersion in the ceria and zirconia promoted Ni/SBA-15 catalyst than Ni/SBA-15 catalyst (Table 1), consistent with TEM observations. From the results of XRD, N$_2$ physisorption, H$_2$-TPR and TEM, it can be inferred that the Ni particles are higher and more homogeneously distributed in Ni/CeO$_2$-SBA-15, Ni/ZrO$_2$-SBA-15 and Ni/CeO$_2$ZrO$_2$-SBA-15 compared to the Ni/SBA-15 catalyst. The ultrasound effect and addition of ceria and zirconia promoter have proved to stabilize the Ni particles and thus inhibit the sintering of Ni particles.

3.2. Catalytic performance for the PG reforming reaction

The catalytic performance for the steam reforming of propylene glycol in microchannel reactors has been studied at 630 °C with a S/C ratio of 3.5, and the resulting conversions are shown in Fig. 6. It can be seen that the Ni/CeO$_2$-SBA-15, Ni/ZrO$_2$-SBA-15 and Ni/CeO$_2$ZrO$_2$-SBA-15 catalysts show highest activity and stability compared to the Ni/SBA-15 catalyst. Moreover, the conversion is constant with no fluctuation during 30 h of reaction time, which exhibits the excellent coking and sintering resistance of the catalysts. The excellent catalytic performance of ceria and zirconia promoted Ni/SBA-15 catalysts could be contributed by two major factors: (i) a high dispersion of small size Ni NPs with intimate interaction between Ni and ceria and/or zirconia promotor that prevent the sintering, and (ii) the richness of surface active oxygen and prolonged metal–support interfacial perimeter that help in the removal of carbon deposits. The surface active oxygen generally consist of two parts, one is surface absorbed oxygen and other is lattice oxygen [56,57]. As seen in Fig. S5, the XP O 1s spectra of CeO$_2$ indicates that surface lattice oxygen (529.6 eV) contributes significantly to reduce the carbon formation on active Ni particles and increases the catalyst stability. The presence of small amounts of ceria and/or zirconia inside the nanochannels of SBA-15 leads to the formation of Ni–Ce and/or −Zr mixed oxides, which expose more active sites to the reactant gases, resulting in higher activity. Wang et al. reported that cerium incorporated into the framework of SBA-15 promoted the formation of metallic Ni particles with smaller size, which prevented the coke deposition [32]. As seen in Fig. 6, Ni/SBA-15 catalyst lost its stability already after 5 h, which results in a decreasing PG conversion. In this case, although the ultrasound treatment controlled the size and dispersion of Ni NPs to some extent, the lack of oxygen mobility deactivates the catalyst quickly and leads to the decreasing catalytic performance. The lower stability of this catalyst is suggested to be caused by sintering, higher coke formation and structural degradation of SBA-
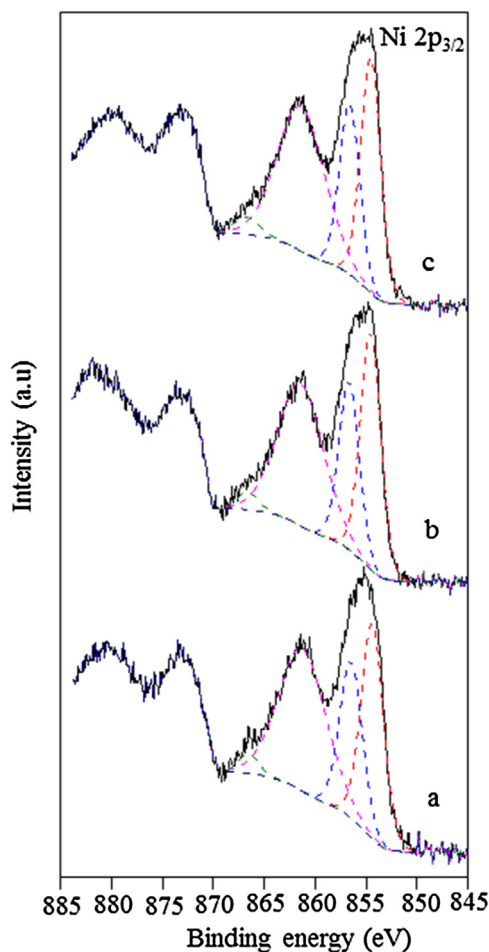
Fig. 3. XP Ni $2p_{3/2}$ spectra of calcined (a) Ni/CeO$_2$-SBA-15, (b) Ni/ZrO$_2$-SBA-15 and (c) Ni/CeO$_2$ZrO$_2$-SBA-15 catalysts.

Fig. 4. H$_2$-TPR profile of (a) Ni/SBA-15, (b) Ni/CeO$_2$-SBA-15, (c) Ni/ZrO$_2$-SBA-15 and (d) Ni/CeO$_2$ZrO$_2$-SBA-15 catalysts.

15 as discussed below in the section about the coke analysis. Xie et al. stated that the Ni impregnated mesoporous silica catalyst shows 33.7% coke deposition, whereas ceria modified-Ni/SiO$_2$ catalyst possesses only 4.2% during the catalytic reforming reaction of methane with carbon dioxide [25]. Li et al. investigated the ethanol reforming reaction over ceria promoted Ni/SBA-15 catalysts. They demonstrated that CeNi/SBA-15 catalyst possesses a 70% lower amount of coke deposition than Ni/SBA-15 evidencing its anti-coking potential by CeO$_2$ addition, which accounts for the excellent long-term stability during ethanol steam reforming reaction [26]. These results are consistent with the present results. In order to investigate the surface active oxygen, we also prepared the catalyst Ni/CuO-SBA-15 with addition of copper (3 wt%) as a promotor (Fig. S6A). This catalyst exhibits poorer catalytic stability than Ni/SBA-15 catalyst, indicating faster deactivation of catalyst due to higher amount of carbon deposited (Fig. S7). The copper oxide might be reduced to metallic copper and developed larger Cu–Ni crystallites responsible for the higher coke content found on this catalyst [37]. When adding a small amount of ceria (1.5 wt%) to the copper containing catalyst (1.5 wt%), to prepare the Ni/CuOCeO$_2$-SBA-15 catalyst, the catalytic stability slightly increased due to the availability of surface active oxygen by CeO$_2$, which enhances the coke resistance (Fig. S6A). The addition of copper as a promotor was found to have a negative effect for the steam reforming of propylene glycol.

Fig. 7 shows the selectivity towards the main products H$_2$ and CO$_2$ as determined under conditions of steam reforming of propylene glycol for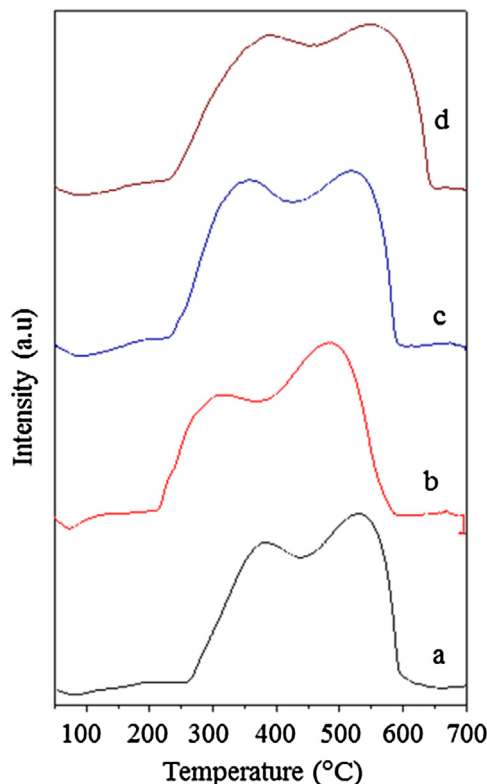 all the catalysts. The selectivity of by-products towards C$_2$H$_4$, C$_2$H$_6$ and C$_3$H$_8$, CO and CH$_4$ are given in Fig. S8. All of the catalysts shows high selectivity towards H$_2$ and CO$_2$. However, the selectivity of H$_2$ and CO$_2$ is slightly higher in Ni/SBA-15 catalyst than for the ceria and zirconia promoted Ni/SBA-15 catalysts. The lower selectivity of H$_2$ and CO$_2$ in ceria and zirconia promoted Ni/SBA-15 catalysts originates probably from the increased selectivity towards C$_3$H$_8$ and C$_2$H$_4$ (see Fig. S8). The selectivity of H$_2$ and CO$_2$ decreases in Ni/CeO$_2$-SBA-15 and Ni/ZrO$_2$-SBA-15 catalysts due to increasing the by-products of C$_2$H$_4$ and C$_3$H$_8$, but Ni/CeO$_2$ZrO$_2$-SBA-15 catalyst shows even more stable behavior, because the selectivity towards C$_2$H$_4$ and C$_3$H$_8$ remains stable compared to the former samples. Although Ni/SBA-15 catalyst showed higher selectivity towards H$_2$, the catalyst lost its stability already after 5 h due to higher carbon deposition. The overall observation has proved that addition of ceria and zirconia promotors plays a vital role in eliminating the carbon deposition deriving from the abundant oxygen vacancies on the surface and inhibit the sintering of Ni NPs through strengthening the interaction between Ni and ceria or zirconia. However, these supports obviously also favour the desorption of the not completely converted light hydrocarbons from the catalyst, which is an undesired effect for the overall reaction. Notably, the Ni/CuO-SBA-15 catalyst (Fig. S6B) shows poor selectivity towards H$_2$ and CO$_2$ due to the reducibility of Cu from CuO species and deactivation of the catalyst; whereas the selectivity towards H$_2$ and CO$_2$ increases on Ni/CuOCeO$_2$-SBA-15 due the presence of CeO$_2$, which suppresses the deactivation through enhanced coking resistance.

3.3. Characteristics of spent catalysts

It is well known that carbon deposition is one of the most important factors of catalyst deactivation. Various characterization techniques were conducted in order to understand the carbon deposition and its effect on catalyst deactivation. First, the TEM
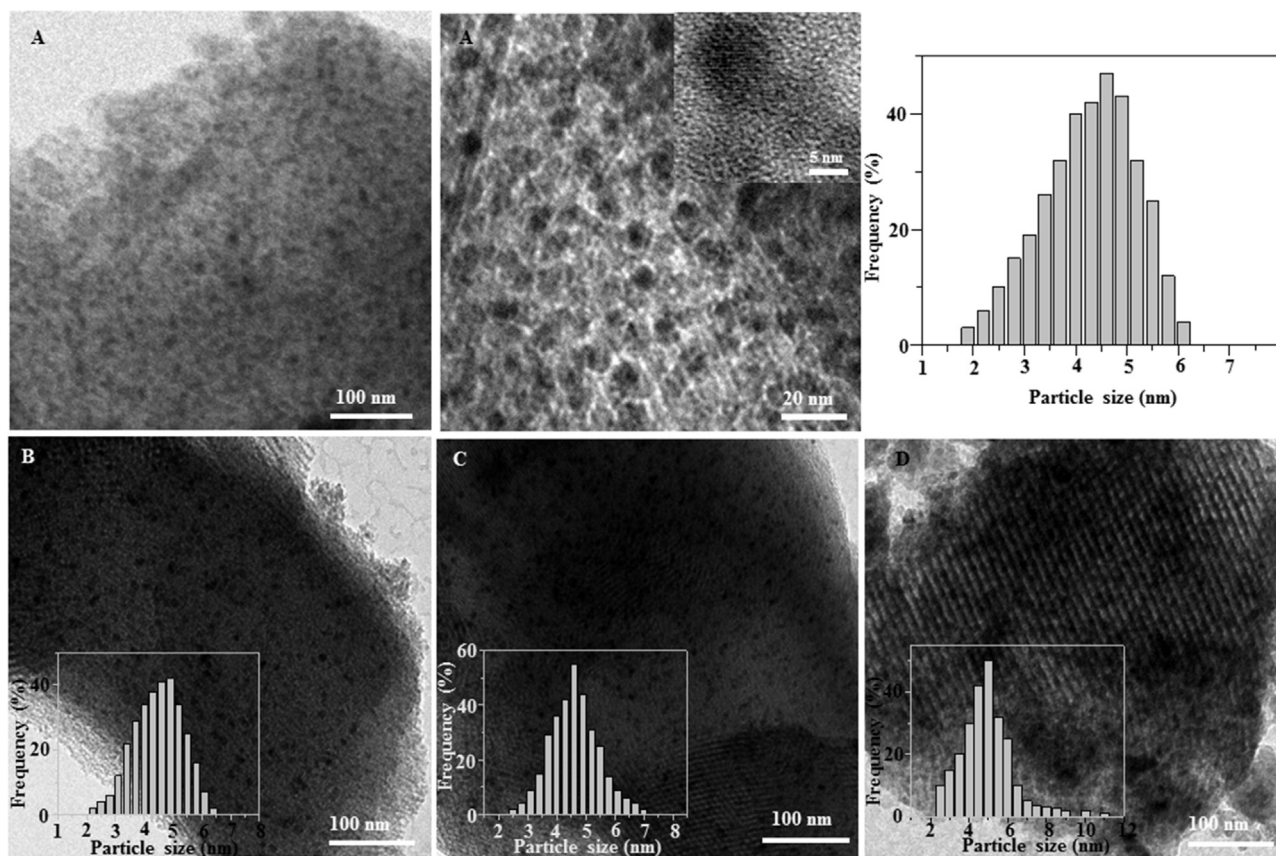
Fig. 5. TEM images of (A) Ni/CeO$_2$-SBA-15, (B) Ni/ZrO$_2$-SBA-15 (C) Ni/CeO$_2$ZrO$_2$-SBA-15 and (D) Ni/SBA-15 catalysts.
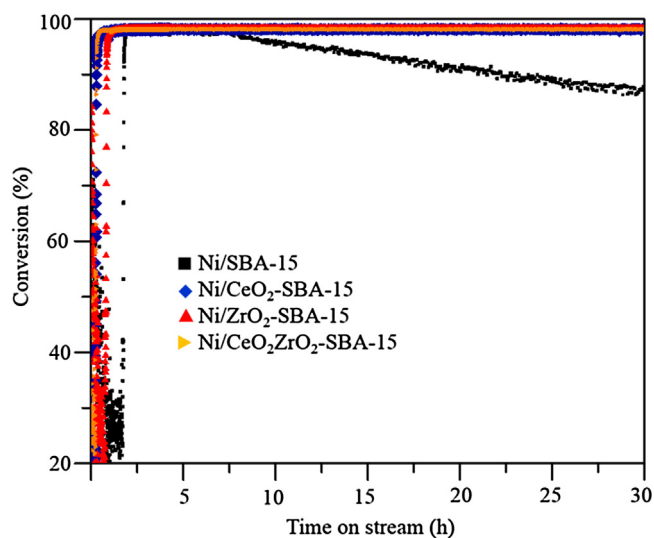

Fig. 6. Steam reforming of PG conversion over Ni/SBA-15, Ni/CeO$_2$-SBA-15, Ni/ZrO$_2$-SBA-15 and Ni/CeO$_2$ZrO$_2$-SBA-15 catalysts.

technique was used to carry out the coke analysis for all the spent catalysts after 30 h of reaction time. Fig. 8 shows the TEM images of spent Ni/SBA-15, Ni/CeO$_2$-SBA-15, Ni/ZrO$_2$-SBA-15 and Ni/CeO$_2$ZrO$_2$-SBA-15 catalysts. It can be seen that the Ni/SBA-15 catalyst presents a large amount of carbon nanotubes or nanofibers with Ni particles at the tips, suggesting that Ni weakly interacting with the silica support has reduced stability under harsh reaction conditions at high temperature. Moreover, the ordered structure of the silica support was destroyed and the agglomerated Ni particles

were found on the outer surface of the mesoporous silica. The Ni particles might have migrated from internal mesopores of silica to the external surface, and otherwise, the structural collapse of the mesoporous silica support might accelerate the sintering of the Ni particles under the reaction conditions. The structural degradation of mesoporous silica support is probably caused by the hydrolysis and rearrangement of surface Si—O—Si bonds under high temperature in presence of steam [24]. It is also possible that the hydroxyl groups of the mesoporous silica support could undergo hydrolysis in presence of steam and the subsequent formed oxygen reacts with carbon in the gasification process of coke [58]. The large size Ni NPs with weak interaction on the external surface of silica are easily encapsulated by carbon layers which induces to grow carbon nanotubes with larger Ni particles at the tips [29], while smaller Ni particles having stronger interaction with silica encourage for base growth of carbon nanotubes as depicted in Fig. 9. The internal diameter of the carbon nanotubes is dependent on the size of Ni nanoparticles. In the case of Ni/CeO$_2$-SBA-15, the hexagonal array of SBA-15 silica is still clearly visible and uniformly filled with Ni NPs indicating the distribution and size of Ni NPs have not been changed significantly, revealing its excellent sintering resistance. However, a few carbon nanotubes have been generated through the diffusion of deposited carbon. The presence of ceria is capable to produce surface Si—O—Ce bonds, which have higher steam resistance than Si—O—Si bonds, and this could prevent the hydrolysis of Si—O—Si bonds under the conditions of high temperature and in presence of steam, leading to a relatively high stability of Ni/CeO$_2$-SBA-15 catalyst [24]. The strong interaction between Ni and ceria and the confinement effect from the mesoporous silica wall suppressed effectively the sintering of Ni particles for Ni/CeO$_2$-SBA-15 catalyst. It has been reported that the carbon deposition was significantly suppressed due to the interaction between Ni particles and ceria or
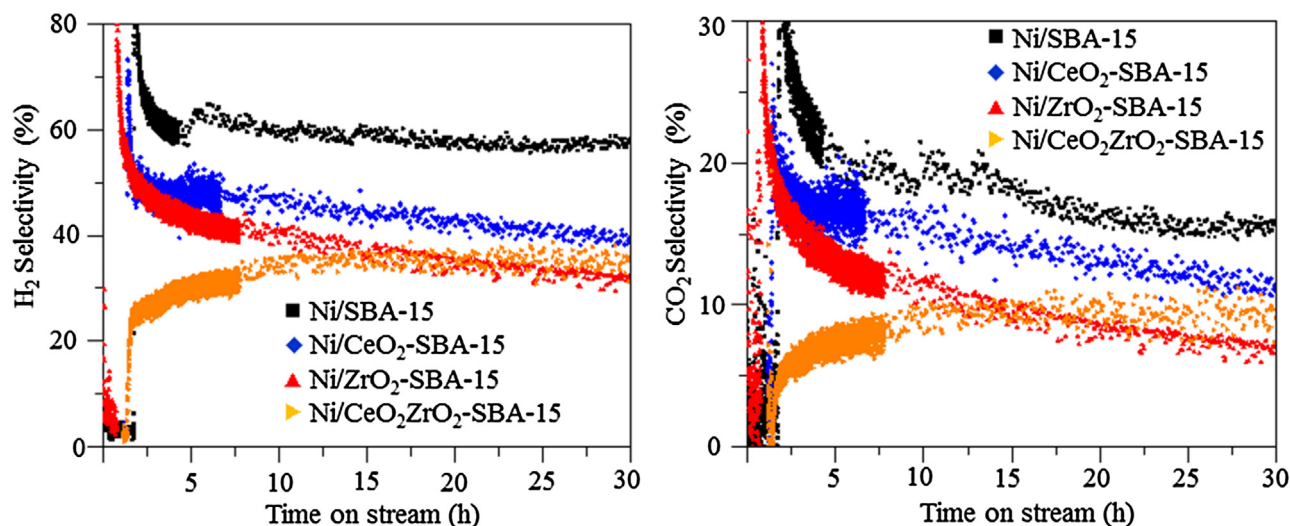
Fig. 7. Steam reforming of H_2 and CO_2 selectivity over Ni/SBA-15, Ni/CeO$_2$-SBA-15, Ni/ZrO$_2$-SBA-15 and Ni/CeO$_2$ZrO$_2$-SBA-15 catalysts.
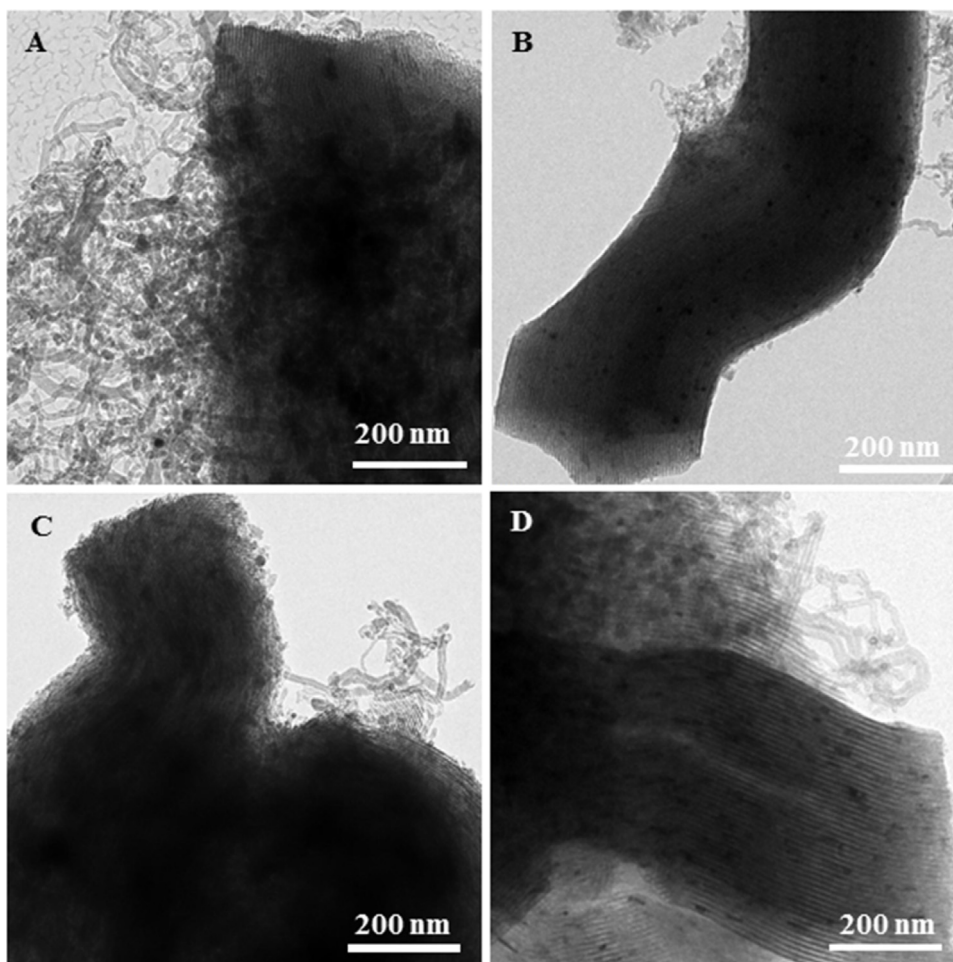

Fig. 8. TEM images of spent (A) Ni/SBA-15, (B) Ni/CeO$_2$-SBA-15, (C) Ni/ZrO$_2$-SBA-15 and (D) Ni/CeO$_2$ZrO$_2$-SBA-15 catalysts.

lanthana species in Ni based Al_2O_3 catalyst modified by CeO_2 and La_2O_3 [59]. Moreover, the addition of ceria considerably enhances both the structural stability of silica and of the active Ni species. As illustrated in Fig. 9, the mobile oxygen released from the ceria lattice could react with carbonaceous species as soon as they deposit on Ni NPs and thus keep the Ni surface free of carbon deposits,

and therefore increased the stability by suppressing catalyst deactivation. The high oxygen storage and transport capacity of ceria prevents the coke deposition via the metal-ceria interface [26]. Similarly, the mesoporous structure still remains and the aggregation of Ni NPs has not occurred on Ni/ZrO$_2$-SBA-15 and Ni/CeO$_2$ZrO$_2$-SBA-15 catalysts. Although some carbon nanotubes have been found on ceria and zirconia promoted Ni/SBA-15 catalysts, the amount
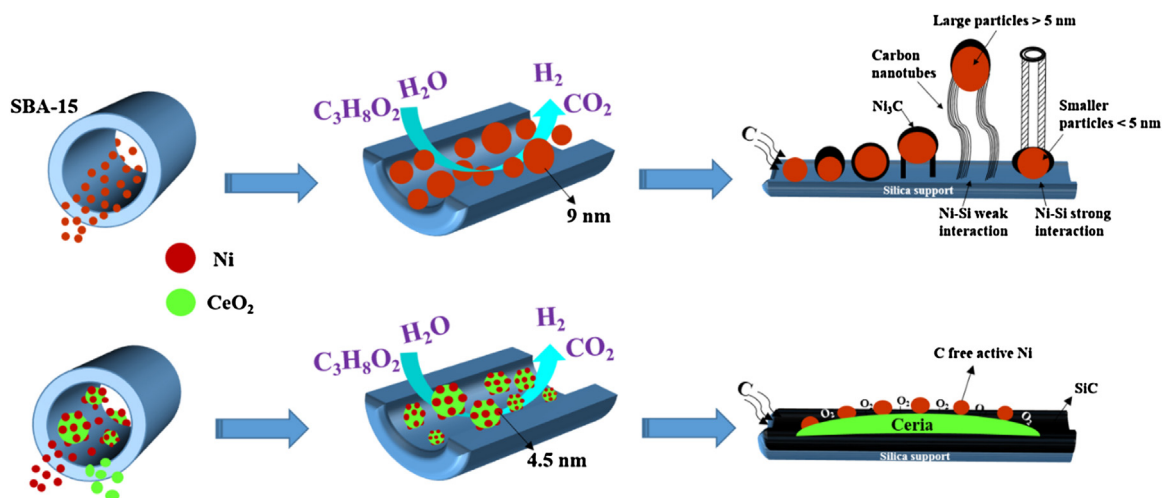
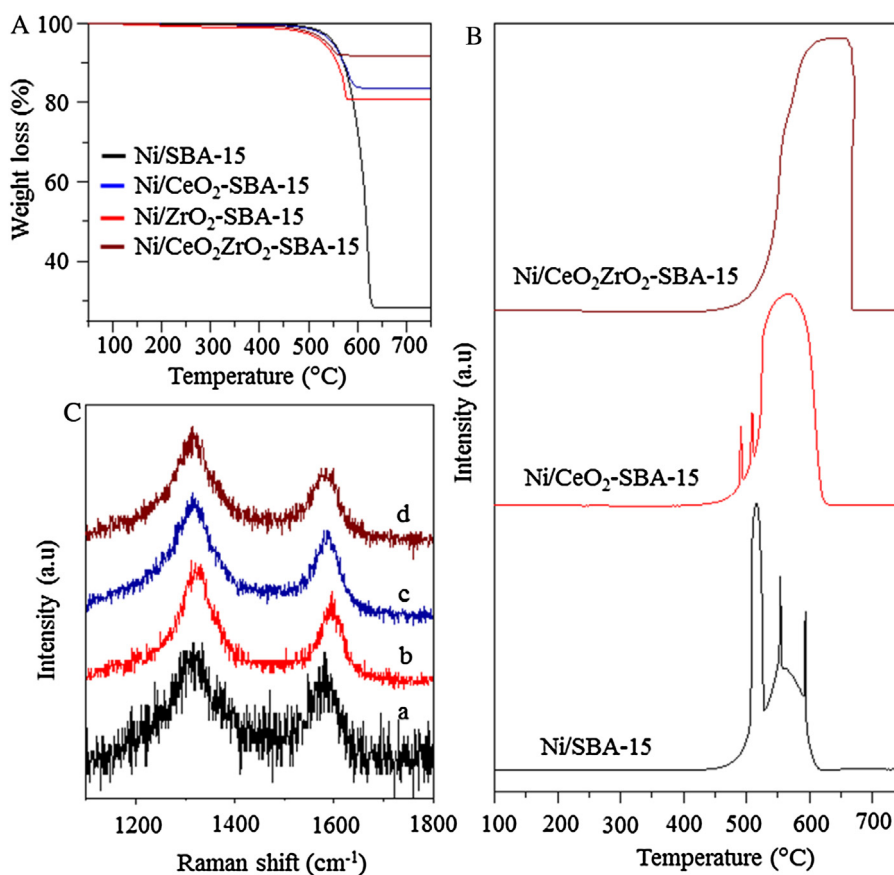**Fig. 9.** Schematic illustration of coke formation mechanism.

Fig. 10. (A) TG analysis of spent Ni/SBA-15, Ni/CeO$_2$-SBA-15, Ni/ZrO$_2$-SBA-15 and Ni/CeO$_2$ZrO$_2$-SBA-15, (B) O$_2$-TPO profile of spent Ni/SBA-15, Ni/CeO$_2$-SBA-15 and Ni/CeO$_2$ZrO$_2$-SBA-15 catalysts and (C) Raman spectra spent a) Ni/SBA-15, (b) Ni/CeO$_2$-SBA-15, (c) Ni/ZrO$_2$-SBA-15 and (d) Ni/CeO$_2$ZrO$_2$-SBA-15 catalysts.

of carbon nanotubes was very small and therefore these catalysts kept constant activity for 30 h. Beyond carbon nanotubes formation, no obvious Ni growth was found on these catalysts, revealing its excellent sintering resistance. The TEM results of spent catalysts have proved that addition of ceria and zirconia inhibits the sintering of Ni NPs due to intimate interaction of Ni with CeO$_2$ or ZrO$_2$, and its higher oxygen storage capacity provides more active oxygen species to prevent carbon formation on these catalysts.

The TG analysis was used to quantify the carbon deposition on spent Ni/SBA-15, Ni/CeO$_2$-SBA-15, Ni/ZrO$_2$-SBA-15 and Ni/CeO$_2$ZrO$_2$-SBA-15 catalysts, and the results are shown in Fig. 10A. For all the above catalysts, no weight loss was observed below 500 °C and the weight loss started decreasing again at 600 °C. The Ni/SBA-15 catalyst showed the highest weight loss of about 71.5%. With addition of ceria and zirconia species, the amount of carbon deposition decreases drastically, and the weight losses of spent Ni/CeO$_2$-SBA-15, Ni/ZrO$_2$-SBA-15 and Ni/CeO$_2$ZrO$_2$-SBA-15 catalysts are 16.5%, 20.4% and 8.2% respectively. The carbon deposited on these three catalyst is more reactive and easily removed by oxidation. The addition of ceria and zirconia promo-

tor not only reduces the rate of coke formation but also accelerates the rate of coke gasification, and consequently leading to good stability for 30 h in the steam reforming of propylene glycol reaction in the microreactor. However, the higher selectivity of these catalysts towards lower hydrocarbons such as ethylene and propane overcompensates the carbon dioxide formation through the carbon gasification and leads to overall lower selectivity towards carbon dioxide, as indicated by the activity tests.

The coke formation on spent Ni/SBA-15, Ni/CeO$_2$-SBA-15 and Ni/CeO$_2$ZrO$_2$-SBA-15 catalysts is evaluated by O$_2$-TPO experiment and results are shown in Fig. 10B. The O$_2$-TPO profile Ni/SBA-15 and Ni/CeO$_2$-SBA-15 shows two peaks in the temparature range between 500 °C and 600 °C representing different carbon deposits on these catalysts. It is acknowledged that the first peak at low temperature corresponds to carbon deposits on active metal, while the second peak at high temperature represents the carbon deposits on the support [60,61]. Accordingly, the Ni/SBA-15 catalyst shows a highly intense peak at 510 °C and a small peak at 570 °C indicating most of the carbon deposited on the Ni surface which decreases the accessability of Ni active sites for the reactant gas in PG reforming reaction, thus resulting in a degradation of catalytic activity and stability. Apparently, a small peak is apprearing at 510 °C and a high intensity peak with large peak area is apprearing at 600 °C for Ni/CeO$_2$-SBA-15 catalyst, evidencing that most of the carbon is deposited on the silica support, as illustrated in Fig. 9, so that Ni actives sites are kept accessible to the reactant gas, and consequenly this catalyst showed longer stable performance than Ni/SBA-15. In the case of Ni/CeO$_2$ZrO$_2$-SBA-15 catalyst, only one peak was observed at a higher temperature of about 600 °C. It is clear that the carbon deposits only on the silica support and not on the Ni particles, and therefore its catalytic performance remains to be excellent as for the Ni/CeO$_2$-SBA-15 catalyst. The results of TEM, TGA and O$_2$-TPO conclude that the ceria and zirconia promoted Ni/SBA-15 catalysts show lower carbon deposition, and even more important less carbon deposited on Ni surface, evidencing the coking prevention potential of ceria and zirconia, which accounts for the excellent activity and stability during propylene glycol steam reforming reaction in the microreactors.

Raman spectrometry is another effective technique to investigate the structure and composition of carbon deposition over spent catalysts. The Raman spectra of spent Ni/SBA-15, Ni/CeO$_2$-SBA-15, Ni/ZrO$_2$-SBA-15 and Ni/CeO$_2$ZrO$_2$-SBA-15 catalysts are presented in Fig. 10C. All of the four catalysts exhibit two major peaks centered approximatly at 1320 cm^{-1} and 1590 cm^{-1}, which are ascribed to D (disorder) and G (graphite) bands of carbon respectively [62]. The D band represents the poorly structured carbon deposits, whereas G band is attributed to well structured coke or graphitic carbon, which derives from the in-plane C—C streching vibrations of pairs of sp^2 carbon [5]. The intensity of the G band over Ni/SBA-15 catalyst which is slighly higher than the D band reveals the presence of more graphitic carbon present in this catalyst. It is worth mentioning that carbon deposition mainly occurs on Ni surface and leads to growth of graphitic carbon, which is the main culprit for catalyst deactivation because it acts like a shell on the catalyst and totally covers the Ni active sites layer by layer [29]. This result is in good agreement with TEM. Interestingly, the intensity of the D band is higher than the G band for Ni/CeO$_2$-SBA-15, Ni/ZrO$_2$-SBA-15 and Ni/CeO$_2$ZrO$_2$-SBA-15 catalysts indicating the presence of more disorder carbonaceous species rather than graphitic carbon. As confirmed with TEM, the disordered carbon could be deposited on the support and few carbon nanotubes formed from Ni NPs weakly interacting with the support. This observation suggests the addition of ceria and zirconia has significant contribution to inhibit the carbon depositon.

4. Conclusion

In conclusion, highly and homogeneously dispersed and size controlled Ni nanoparticles in CeO$_2$ and ZrO$_2$ promoted mesoporous SBA-15 silica have been successfully prepared by the ultrasound treatment, and investigated for the steam reforming of propylene glycol in microreactors. Characterization results have confirmed that the addition of ceria and zirconia into SBA-15 plays a vital role to control the size and promote the dispersion of Ni NPs into the mesoporous nanochannels with the aid of ultrasound. The ceria and zirconia promoted Ni/SBA-15 catalysts have shown superior catalytic stability in propylene glycol reforming reaction than Ni/SBA-15, owing to its highest Ni active surface and largest Ni-CeO$_2$ or ZrO$_2$ interfacial area. The confined ceria and zirconia increased the Ni-CeO$_2$ or ZrO$_2$ interaction, which obviously restrict the sintering of Ni NPs along with a confinement effect arising from the pore wall of the silica support under harsh reaction condition, revealing the excellent sintering resistance of ceria and zirconia promoted Ni/SBA-15 catalysts. Furthermore, the higher mobility of surface oxygen species of ceria and zirconia promoted Ni/SBA-15 catalysts inhibited the carbon deposition on the Ni surface and enhanced the coke resistance of these catalysts. On the other hand, the excellent heat transfer efficiency of microreactor makes the temperature highly uniform across the catalyst coating layer, which inhibits the existence of hot-spot temperature. Thus, the coke formation is restrained effectively leading to stable performance during long time runs. This combination of metal oxide promotors and ultrasound treatment strategies can be applied to develop other relevant well-dispersed metal particles in nanochannels of mesoporous silica, which can be applied in many other reforming reactions which are critical concerning coke formation and sintering.

Acknowledgements

Appendix A. Supplementary data

Supplementary data associated with this article can be found, in the online version, at http://dx.doi.org/10.1016/j.apcatb.2016.10.075.

References

[1] M. Momirlan, T.N. Veziroglu, Int. J. Hydrogen Energy 30 (2005) 795–802.
[2] C. Qi, J.C. Amphlett, B.A. Peppley, Catal. Lett. 104 (2005) 57–62.
[3] S. He, S. He, L. Zhang, X. Li, J. Wang, D. He, J. Lu, Y. Luo, Catal. Today 258 (2015) 162–168.
[4] S. Li, C. Zhang, P. Zhang, G. Wu, X. Ma, J. Gong, Phys. Chem. Chem. Phys. 14 (2012) 4066–4069.
[5] L. Yerman, N. Homs, E.B. Pereira, P. Ramírez de la Piscina, Int. J. Hydrogen Energy 39 (2014) 5225–5233.
[6] J.A. Calles, A. Carrero, A.J. Vizcaino, L. Garcia-Moreno, Catal. Today 227 (2014) 198–206.
[7] P.D. Vaidya, A.E. Rodrigues, Chem. Eng. Technol. 10 (2009) 1463–1469.
[8] D. Li, X. Li, J. Gong, Chem. Rev. 116 (2016) 11529–11653.
[9] H. Tian, X. Li, L. Zeng, J. Gong, ACS Catal. 5 (2015) 4959–4977.
[10] S.D. Davidson, H. Zhang, J. Sun, Y. Wang, Dalton Trans. 43 (2014) 11782–11802.
[11] N. Wang, Z. Xu, J. Deng, K. Shen, X. Yu, W. Qian, W. Chu, F. Wei, ChemCatChem 6 (1) (2014) 1470–1480.
[12] N. Wang, K. Shen, L. Huang, X. Yu, W. Qian, W. Chu, ACS Catal. 3 (2013) 1638–1651.

[13] S.J. Han, Y. Bang, J. Yoo, J.G. Seo, I.K. Song, Int. J. Hydrogen Energy 38 (2013) 8285–8292.
[14] A. Carrero, J.A. Calles, A.J. Vizcaino, Appl. Catal. A: Gen. 327 (2007) 82–94.
[15] J.W. Han, C. Kim, J.S. Park, H. Lee, ChemSusChem 7 (2014) 451–456.
[16] W. Shen, K. Komatsubara, T. Hagiyama, A. Yoshida, S. Naito, Chem. Commun. (2009) 6490–6492.
[17] S. Li, J. Gong, Chem. Soc. Rev. 43 (2014) 7245–7256.
[18] H. Friedrich, J.R.A. Sietsma, P.E. de Jongh, A.J. Verkleij, K.P. de Jong, J. Am. Chem. Soc. 129 (2007) 10249–10254.
[19] C.J. Liu, J. Ye, J. Jiang, Y. Pan, ChemCatChem 3 (2011) 529–541.
[20] M. Lindo, A.J. Vizcaino, J.A. Calles, A. Carrero, Int. J. Hydrogen Energy 35 (2010) 5895–5901.
[21] T. Xie, L. Shi, J. Zhang, D. Zhang, Chem. Commun. 50 (2014) 7250–7253.
[22] D. Baudouin, U. Rodemerck, F. Krumeich, A.d. Mallmann, K.C. Szeto, H. Menard, L. Veyre, J.-P. Candy, P.B. Webb, C. Thieuleux, C. Coperet, J. Catal. 297 (2013) 27–34.
[23] J.H. Kim, D.J. Suh, T.-J. Park, K.L. Kim, Appl. Catal. A 197 (2000) 191–200.
[24] S. Zhang, S. Muratsugu, N. Ishiguro, M. Tada, ACS Catal. 3 (2013) 1855–1864.
[25] T. Xie, X. Zhao, J. Zhang, L. Shi, D. Zhang, Int. J. Hydrogen Energy 40 (2015) 9685–9695.
[26] D. Li, L. Zeng, X. Li, X. Wang, H. Ma, S. Assabumrungrat, J. Gong, Appl. Catal. B: Environ. 176–177 (2015) 532–541.
[27] A.J. Vizcaino, A. Carrero, J.A. Calles, Int. J. Hydrogen Energy 32 (2007) 1450–1461.
[28] F. Habimana, X. Li, S. Ji, B. Lang, D. Sun, C. Li, J. Nat. Gas Chem. 18 (2009) 392–398.
[29] T. Huang, W. Huang, J. Huang, P. Ji, Fuel Process. Technol. 92 (2011) 1868–1875.
[30] D. Kim, B.S. Kwak, N.K. Park, G.B. Han, M. Kang, Int. J. Energy Res. 39 (2015) 279–292.
[31] H. Zhang, M. Li, P. Xiao, D. Liu, C.J. Zou, Chem. Eng. Technol. 36 (2013) 1701–1707.
[32] N. Wang, W. Chu, T. Zhang, X.S. Zhao, Int. J. Hydrogen Energy 37 (2012) 19–30.
[33] K. Wang, X. Li, S. Ji, X. Shi, J.J. Tang, Energy Fuels 23 (2009) 25–31.
[34] A. Albarazi, M.E. Galvez, P.D. Costa, Catal. Commun. 59 (2015) 108–112.
[35] J. Tao, L. Zhao, C. Dong, Q. Lu, X. Du, E. Dahlquist, Energies 6 (2013) 3284–3296.
[36] A. Albarasi, M.E. Galvez, P.D. Costa, Int. J. Hydrogen Energy 38 (2013) 127–139.
[37] J.A. Calles, A. Carrero, A.J. Vizcaíno, Microporous Mesoporous Mater. 119 (2009) 200–207.
[38] H. Wan, X. Li, S. Ji, B. Huang, K. Wang, C. Li, J. Nat. Gas Chem. 16 (2007) 139–147.
[39] D. Liu, X.Y. Quek, H.H.A. Wah, G. Zeng, Y. Li, Y. Yang, Catal. Today 148 (2009) 243–250.
[40] Q.S. Jing, X.M. Zheng, Energy 31 (2006) 2184–2192.
[41] S. Seok, M.A. Hussain, K.J. Park, J.W. Kim, D.H. Kim, Ultra. Sonochem. 28 (2016) 178–184.
[42] V. Shanmugam, S. Neuberg, R. Zapf, V. Hessel, G. Kolb, Catal. Commun. 83 (2016) 43–47.
[43] G. Kolb, V. Hessel, Chem. Eng. J. 98 (2004) 1–38.
[44] G. Kolb, Chem. Eng. Process. 65 (2013) 1–44.
[45] D.Y. Zhao, J.L. Feng, Q.S. Huo, N. Melosh, G.H. Fredrickson, B.F. Chmelka, G.D. Stucky, Science 279 (1998) 548–552.
[46] R. Zapf, C. Becker-Willinger, K. Berresheim, H. Bolz, H. Gnaser, V. Hessel, G. Kolb, P. Löb, A.-K. Pannwitt, A. Ziogas, Chem. Eng. Res. Des. 81 (2003) 721–729.
[47] G. Kolb, R. Zapf, V. Hessel, H. Löwe, Appl. Catal. A 277 (2004) 155–166.
[48] U. Izquierdo, M. Wichert, G. Kolb, V.L. Barrio, R. Zapf, A. Ziogas, S. Neuberg, P.L. Ariasa, J.F. Cambra, Int. J. Hydrogen Energy 39 (2014) 5248–5256.
[49] M.Y. Cheng, C.J. Pan, B.J. Hwang, J. Mater. Chem. 19 (2009) 5193–5200.
[50] D.R. Burri, K.M. Choi, J.H. Lee, D.S. Han, S.E. Park, Catal. Commnun. 8 (2007) 43–48.
[51] D. Kim, B.S. Kwak, N.K. Park, G.B. Han, M. Kang, Int. J. Energy Res. 39 (2015) 279–292.
[52] M. Mureddu, I. Ferino, A. Musinu, A. Ardu, E. Rombi, M.G. Cutrufello, P. Deiana, M. Fantauzzia, C. Cannas, J. Mater. Chem. A 2 (2014) 19396–19406.
[53] J.R.A. Sietsma, H. Friedrich, A. Broersma, M. Versluijs-Helder, A. Jos van Dillen, P.E. de Jongh, K.P. de Jong, J. Catal. 260 (2008) 227–235.
[54] Y.M. Dai, C.Y. Lu, C.J. Chang, RSC Adv. 6 (2016) 73887–73896.
[55] R. Gomez-Reynoso, J. Ramırez, R. Nares, R. Luna, F. Murrieta, Catal. Today 107–108 (2005) 926–932.
[56] D. He, G. Wan, H. Hao, D. Chen, J. Lu, L. Zhang, F. Liu, L. Zhong, S. He, Y. Luo, Chem. Eng. Journal 289 (2016) 161–169.
[57] R. Yu, L. Yan, P. Zheng, J. Chen, X. Xing, J. Phys. Chem. C 112 (2008) 19896–19900.
[58] Y. Matsumura, T. Nakamori, Appl. Catal. A 258 (2004) 107–114.
[59] P.O. Vargas, N.A.F. González, R.M. Navarro, J.L.G. Fierro, C.H. Campos, P. Reyes, Catal. Today 259 (2015) 27–38.
[60] S.M. Stagg-Williams, F.B. Noronha, G. Fendley, D.E. Resasco, J. Catal. 194 (2000) 240–249.
[61] A.N. Fatsikostas, X.E. Verykios, J. Catal. 225 (2004) 439–452.
[62] S. Vetrivel, J.S. Do, M.Y. Cheng, B.J. Hwang, J. Phys. Chem. C 111 (2007) 16211–16218.